

Giant magnetochiral anisotropy from quantum confined surface states of topological insulator nanowires

Henry F. Legg,^{1,*} Matthias Röbler,^{2,*} Felix Munning,² Dingxun Fan,² Oliver Breunig,² Andrea Bliesener,² Gertjan Lippertz,^{2,3} Anjana Uday,² A. A. Taskin,² Daniel Loss,¹ Jelena Klinovaja,¹ and Yoichi Ando²

¹*Department of Physics, University of Basel, Klingelbergstrasse 82, CH-4056 Basel, Switzerland*

²*Physics Institute II, University of Cologne, Zùlpicher Str. 77, 50937 Köln, Germany*

³*KU Leuven, Quantum Solid State Physics, Celestijnenlaan 200 D, 3001 Leuven, Belgium*

Wireless technology relies on the conversion of alternating electromagnetic fields to direct currents, a process known as rectification. While rectifiers are normally based on semiconductor diodes, quantum mechanical non-reciprocal transport effects that enable highly controllable rectification have recently been discovered^{1–5}. One such effect is magnetochiral anisotropy (MCA)^{3–5}, where the resistance of a material or a device depends on both the direction of current flow and an applied magnetic field. However, the size of rectification possible due to MCA is usually extremely small, because MCA relies on electronic inversion symmetry breaking which typically stems from intrinsic spin-orbit coupling – a relativistic effect – in a non-centrosymmetric environment^{3–5}. Here, to overcome this limitation, we artificially break inversion symmetry via an applied gate voltage in thin topological insulator (TI) nanowire heterostructures and theoretically predict that such a symmetry breaking can lead to a giant MCA effect. Our prediction is confirmed via experiments on thin bulk-insulating $(\text{Bi}_{1-x}\text{Sb}_x)_2\text{Te}_3$ TI nanowires, in which we observe the largest ever reported size of MCA rectification effect in a normal conductor – over 10000 times greater than in a typical material with a large MCA^{5–7} – and its behaviour is consistent with theory. Our findings present new opportunities for future technological applications of topological devices.

In most materials, transport is well described by Ohm’s law, $V = IR_0$, dictating that for small currents I the voltage drop across a material is proportional to a constant resistance R_0 . Junctions that explicitly break inversion symmetry, for instance semiconductor pn -junctions, can produce a difference in resistance R as a current flows in one or the opposite direction through the junction, $R(+I) \neq R(-I)$; this difference in resistance is the key ingredient required to build a rectifier. A much greater degree of control over the rectification effect can be achieved when a similar non-reciprocity of resistance exists as a property of a material rather than a junction. However, to achieve such a non-reciprocity necessi-

tates that the inversion symmetry of the material is itself broken. Previously, the largest non-reciprocal resistivity effects were observed in materials where electronic inversion symmetry was broken by strong intrinsic spin-orbit coupling (SOC)^{3–8}. However, since SOC is always a very small energy scale, this severely limits the possible size of any rectification effect and also potential technological applications. In heterostructures of topological materials, it is possible to artificially break the inversion symmetry of a material⁹ – such an approach provides an unexplored playground to significantly enhance the size of non-reciprocal transport effects. Utilising this idea of artificial symmetry breaking, we will show both theoretically and experimentally that breaking inversion symmetry in a topological insulator nanowire device, achieved here via the application of a gate voltage to the top of the nanowire, leads to a huge rectification effect that is several orders of magnitude larger than previously observed in a normal conductor.

The non-reciprocal transport effect considered here is magnetochiral anisotropy (MCA), which can occur only when both inversion and time-reversal symmetry are broken^{3–8}. When allowed, the leading order correction of Ohm’s law due to MCA is a term second order in current and manifests itself as a resistance of the form $R = R_0(1 + \gamma BI)$, with B the magnitude of an external magnetic field and where γ determines the size of the possible rectification effect. Up to now, even in systems where the inversion symmetry breaking due to SOC was largest, γ is still found to be extremely small and in normal conductors almost always at most⁷ $|\gamma| \sim 1 \text{ A}^{-1}\text{T}^{-1}$. The largest MCA effects previously observed were in the topological semi-metal ZrTe_5 and in chiral carbon nanotubes where $|\gamma| \sim 100 \text{ A}^{-1}\text{T}^{-1}$ have been reported^{8,10}, in the latter case this was largely due to the fact that a nanotube can be considered a quasi one-dimensional (1D) system. In this context, thin bulk-insulating three-dimensional TI nanowires are a perfect platform to investigate the large possible MCA effects due to artificial inversion symmetry breaking. When no symmetry breaking is present, the surface states of a TI nanowire wrap around the cross-section forming spin-degenerate quasi-1D subbands of states with momentum parallel to the wire axis and quantised angular momentum around the nanowire^{9,11–14}. When, in addition, inversion symmetry is broken by a gate voltage applied to one side (see Fig. 1), the spin-degeneracy of quasi-1D subbands is lifted for finite momenta⁹. We will show that this subband split-

* These authors contributed equally

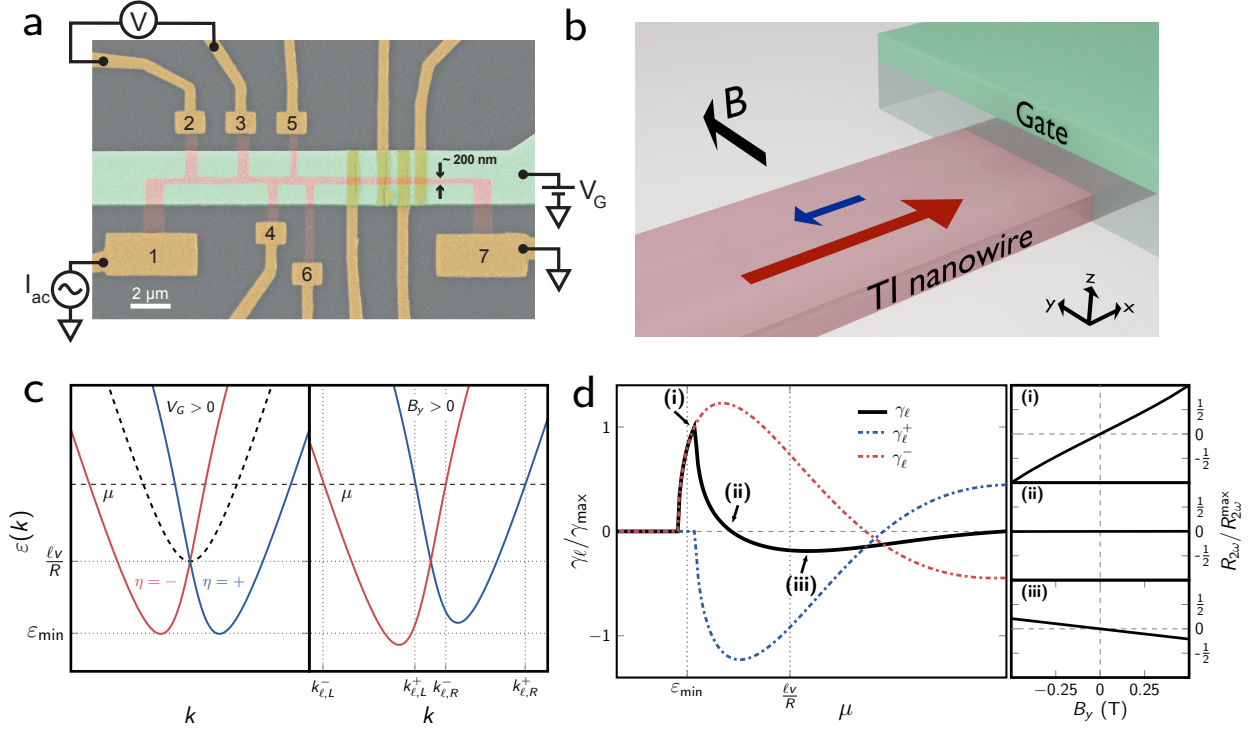


FIG. 1: **Gate-tunable topological insulator nanowire device and the theory of magnetochiral anisotropy:** **a**, False-colour scanning-electron-microscope image of Device 1 with schematics of the electrical wiring; the Pt/Au leads are coloured in dark yellow, the TI nanowire etched from an MBE-grown BST thin film in red, and the top-gate electrode in green. The resistance of the nanowire was measured on different sections: Section 1, 2, 3, 4, 5 correspond to the voltage-contact pairs 2-3, 3-4, 4-5, 5-6, and 2-6, respectively. **b**, Schematic of MCA in TI nanowires. A gate, applied here to the top of the nanowire, breaks inversion symmetry along the wire. Applying a magnetic field perpendicular to the gate normal and the nanowire (y -direction) results in a giant MCA rectification such that current flows more easily in one direction along the wire than the opposite (indicated by red/blue arrows). **c**, TI nanowire surface states form degenerate subbands (dashed line). When a finite gate voltage is applied, inversion symmetry is broken and the subbands split (solid lines). A new minimum occurs at ϵ_{\min} and the states possess a finite spin polarisation in the y -direction (red/blue colour). Applying a magnetic field B_y parallel or anti-parallel to this spin polarisation shifts the subband pair relative to each other in energy due to the Zeeman effect and enables an MCA (the size of the shift shown here is not to scale and used for clarity). **d**, Size of the MCA rectification γ_ℓ (see Eq. (1)) as a function of chemical potential μ within a given subband pair. Due to the peculiar dispersion of a TI nanowire, the curvature, $\hbar^2 \mathcal{V}_\ell^\eta(k) \equiv \partial_k^2 \epsilon_\ell^\eta(k)$, is large and highly anisotropic at opposite Fermi momenta resulting in a giant MCA. As the chemical potential μ is tuned from the bottom of the subband, γ_ℓ changes sign. Here, for clarity, we used $B = 1$ T, see Supplementary Information for further parameters. The sub-panels i-iii) show the theoretically expected magnetic-field dependence of the 2nd harmonic resistance $R_{2\omega}$ at the chemical potentials indicated in the main panel.

ting can be expected to give rise to a giant MCA. We confirm our theoretical prediction by the measurement of an MCA in thin $(\text{Bi}_{1-x}\text{Sb}_x)_2\text{Te}_3$ TI nanowires where we find a giant MCA consistent with the theoretically predicted behaviour in all measured devices and with a rectification effect up to $|\gamma| \approx 6 \times 10^4 \text{ A}^{-1}\text{T}^{-1}$, hundreds of times larger than the largest previously observed MCA effects.

Theory. For an idealised cylindrical TI nanowire – although generalisable to an arbitrary cross-section^{9,13} – the surface states form energy subbands of momentum k along the nanowire and half-integer angular momentum $\ell = \pm\frac{1}{2}, \frac{3}{2}, \dots$ around the nanowire, where the half-integer values are due to spin-momentum locking. The presence of inversion symmetry along a TI nanowire re-

quires that the subbands with angular momenta $\pm\ell$ are degenerate. It is possible to break this inversion symmetry along the wire artificially by application of a gate-voltage from the top of the TI nanowire^{9,12,14}. Such a gate voltage induces a non-uniformity of charge density across the nanowire cross-section which breaks the subband degeneracy and results in a splitting of the subband at finite momenta⁹ (see Fig. 1c). An additional consequence is that the subband states develop finite spin polarisation in the direction perpendicular to the normal of the gate and nanowire axis (y -direction) with the states with opposite momenta being polarized in the opposite directions such that the time-reversal symmetry is respected. If a magnetic field is applied parallel to this direction, the subbands can be shifted in energy

via the Zeeman effect, which suggests that an MCA can be present in this setup. Indeed, using the Boltzmann equation^{6–8} (see Supplementary Information), we find an MCA of the vector product type $\gamma \propto \mathbf{P} \cdot (\hat{\mathbf{B}} \times \hat{\mathbf{I}})$, where $\mathbf{P} \parallel \hat{\mathbf{z}}$ is a vector that characterises the electronic inversion symmetry breaking. For the rectification effect $\gamma_\ell(\mu)$ of a given subband pair $\eta = \pm$ labelled by $\ell > 0$, we find (see Methods and Supplementary Information for details)

$$\gamma_\ell = \gamma_\ell^+ + \gamma_\ell^- \approx \frac{e^3}{(\sigma^{(1)})^2 h B} \sum_{\eta=\pm} \tau^2 \left[\mathcal{V}_\ell^\eta(k_{\ell,R}^\eta) - \mathcal{V}_\ell^\eta(k_{\ell,L}^\eta) \right], \quad (1)$$

where e is the elementary charge, h is the Planck constant, $\sigma^{(1)}$ is the conductivity in linear response, τ is the scattering time, $\mathcal{V}_\ell^\eta(k) = \frac{1}{\hbar^2} \partial_k^2 \varepsilon_\ell^\eta(k)$ with $\varepsilon_\ell^\eta(k)$ describing the energy spectrum in the presence of symmetry breaking terms and of the finite magnetic field B (see Fig. 1c and Supplementary Information), and $k_{\ell,R(L)}^\eta$ is the right (left) Fermi momentum of a given subband (see Fig. 1c). Due to the non-parabolic spectrum of subbands, $\mathcal{V}_\ell^\pm(k)$ is large for a TI nanowire resulting in the giant MCA (see Supplementary Information). The quantities γ_ℓ^+ and γ_ℓ^- are the contributions of the individual subbands. The behaviour of γ_ℓ as a function of chemical potential μ is shown in Fig. 1d. We find that, as the chemical potential is tuned through the subband pair, γ_ℓ will change sign depending on the chemical potential. This makes the rectification effect due to the MCA highly controllable by both magnetic field direction and by the chemical potential μ within a given subband pair, which can be experimentally adjusted by small a change in gate voltage. For reasonable experimental parameters we predict that the theoretical size of the rectification can easily reach giant values $\gamma \sim 5 \times 10^5 \text{ T}^{-1} \text{ A}^{-1}$ (see Supplementary Information), which would be orders of magnitude larger than any previously observed MCA rectification effect in a normal conductor^{3–8}.

Experiment. To experimentally investigate the predicted non-reciprocal transport behaviour, we fabricated nanowire devices¹⁵ of the bulk-insulating TI material $(\text{Bi}_{1-x}\text{Sb}_x)_2\text{Te}_3$ as shown in Fig. 1a by etching high-quality thin films grown by molecular beam epitaxy (MBE). The nanowires have a rectangular cross-section of height $h \approx 16 \text{ nm}$ and width $w \approx 200\text{--}300 \text{ nm}$, with channel lengths up to several μm . An electrostatic gate electrode is placed on top of the transport channel for the dual purpose of breaking inversion symmetry and tuning the chemical potential. The resistance R of the nanowire shows a broad maximum as a function of the gate voltage V_G (see Fig. 2a inset), which indicates that the chemical potential can be tuned across the charge neutrality point (CNP) of the surface state Dirac-cone. Near the broad maximum (i.e. around the CNP), the V_G dependence of R shows reproducible peaks and dips (see Fig. 2a), which occur due to the increased scattering close to subband minima¹⁴. To measure the non-reciprocal transport, we used a low-frequency ac excitation current $I = I_0 \sin \omega t$ and probed the second-harmonic re-

sistance $R_{2\omega}$. The MCA causes a second-harmonic signal that is antisymmetric with magnetic field \mathbf{B} , and therefore we calculated the antisymmetric component $R_{2\omega}^A \equiv \frac{R_{2\omega}(\mathbf{B}) - R_{2\omega}(-\mathbf{B})}{2}$, which is proportional to γ via $R_{2\omega}^A = \frac{1}{2} \gamma R_0 B I_0 \approx \frac{1}{2} \gamma R B I_0$, where R_0 is the reciprocal resistance (see Methods for details).

As predicted by theory, we observed a large $R_{2\omega}^A$ for $V_G \gtrsim 2 \text{ V}$ with a magnetic field perpendicular to the current and gate normal. The $R_{2\omega}^A(B_y)$ behaviour is linear for small B_y (see Fig. 2b) and $R_{2\omega}^A$ increases linearly with I_0 up to $\sim 250 \text{ nA}$ (see Fig. 2c), both of which are the defining characteristics of the MCA. The magnetic-field-orientation dependence of γ , shown in Fig. 2d for in-plane rotation, agrees well with $\gamma \approx \gamma_0 \cos \alpha$, with α the angle from the y -direction and γ_0 the value at $\alpha = 0$; out-of-plane rotation gave similar results (see Supplementary Information). This is consistent with the vector-product type MCA, $R_{2\omega}^A \propto \mathbf{P} \cdot (\mathbf{B} \times \mathbf{I})$, with the orientation of the inversion-symmetry-breaking vector \mathbf{P} parallel to the gate normal, as expected. The maximum size of the $|\gamma|$ in Fig. 2d reaches a giant value of $|\gamma| \sim 6 \times 10^4 \text{ A}^{-1} \text{ T}^{-1}$, which is several orders of magnitude larger than any previously reported value for a normal conductor^{3–8}. In addition, one may notice in Figs. 2b and 2d that the relative sign of γ changes for different V_G values, which is very unusual. We observe a giant MCA with similarly large rectification γ in all measured devices (see Supplementary Information).

A unique feature of the predicted MCA is the controllability of its sign with a small change of V_G . To confirm this prediction, we measured detailed V_G -dependence of $R_{2\omega}^A$ in the V_G range of 5.1–5.5 V, where the chemical potential appears to pass through two subband minima, because $R(V_G)$ presents two peaks (see Fig. 3a). We indeed observe the slope of $R_{2\omega}^A(B_y)$ to change sign with V_G (see Fig. 3b), and its zero-crossing roughly coincides with the peak or dip in the $R(V_G)$ curve (compare Figs. 3a and 3b). A change in sign of the slope of $R_{2\omega}^A(B_y)$ on either side of $R(V_G)$ peaks is also observed in other devices (see Supplementary Information). To obtain confidence in this striking observation, the evolution of the $R_{2\omega}^A(B_y)$ behaviour upon changing V_G is shown in Fig. 3c for many V_G values. This sign change upon a small change of gate voltage also endows the giant MCA in TI nanowires with an unprecedented level of control.

Discussion. The presence of the giant MCA provides compelling evidence for a large spin-splitting of the subbands in TI nanowires with broken inversion symmetry. This spin-splitting has many potential applications, for instance, the nearly perfect helical spin polarization of the split subbands could be used as spin-filters^{16,17} or for other spintronics applications. Recently, it has also been suggested that the helical spin polarization and large energy scales possible in such TI nanowires with broken inversion symmetry could provide a new experimental platform for Majorana bound states⁹ which are an integral building block for future topological quantum computers.

The giant MCA observed here due to an artificial

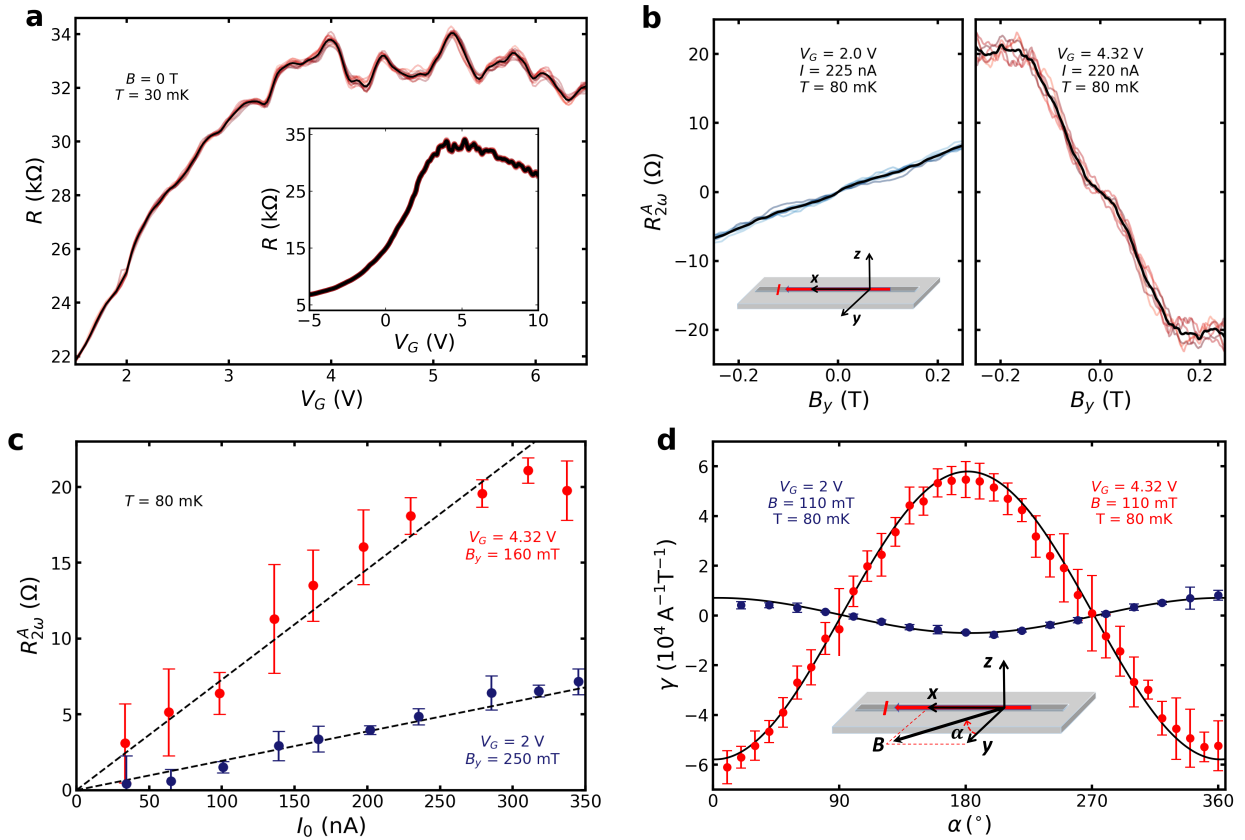


FIG. 2: **Non-reciprocal transport in $(\text{Bi}_{1-x}\text{Sb}_x)_2\text{Te}_3$ topological insulator nanowire:** **a**, Four-terminal resistance R measured on Device 1, Section 1, at 30 mK in 0 T as a function of gate voltage V_G showing reproducible peaks and dips around the resistance maximum, which are consistent with the response expected from quantum-confined surface states¹⁴. Since the R value is very sensitive to the details of the charge distributions in/near the nanowires, the $R(V_G)$ behaviour is slightly different for different sweeps; thin red lines show the results of 15 uni-directional V_G sweeps and the thick black line shows their average. Inset shows the data for a wider range of V_G , demonstrating the typical behaviour of a bulk-insulating TI. **b**, Antisymmetric component of the second-harmonic resistance, $R_{2\omega}^A$, for $V_G = 2$ and 4.32 V plotted vs magnetic field \mathbf{B} applied along the y -direction (coordinate system is depicted in the inset); coloured thin lines show 6 individual B -field sweeps and the thick black line shows their average. **c**, $R_{2\omega}^A$ measured for $V_G = 2$ and 4.32 V in the B -field (applied in the y -direction) of 0.25 and 0.16 T, respectively, as a function of the ac excitation current I_0 . The dashed lines are a guide to the eye marking the linear behaviour. **d**, Magnetic-field-orientation dependencies of γ at $V_G = 2$ V (blue) and 4.32 V (red) when the B -field is rotated in the plane of the film (i.e. xy -plane); error bars are defined by the Min-Max method. Solid black lines are fits to $\gamma \approx \gamma_0 \cos \alpha$ expected for MCA. The inset shows the definition of α and the coordinate system.

breaking of inversion symmetry in topological insulator nanowires opens new pathways to explore non-reciprocal transport effects in topological devices. Not only is the maximum rectification γ observed in a TI orders of magnitude larger than any previously reported, but the giant MCA effect in TI nanowires is also highly controllable by small changes of chemical potential. Although rather different to the MCA of a normal conductor discussed here, we note that the huge size of the rectification effect in a TI nanowire can be similar in magnitude to that recently discovered in non-centrosymmetric superconductor devices¹, where the controllability is comparatively limited.

TI nanowire devices are still in their infancy¹⁵ and so the size of MCA could be increased, perhaps substantially, with future improvements in nanowire quality that will enable an increase of the relevant energy scales closer to the theoretical limit. In principle, the temperature at which giant MCA in TI nanowires is observable is limited only by the subband gap, which is larger in thinner/narrower nanowires. As such, the giant MCA discovered here could provide a pathway to almost full rectification at relatively high temperatures.

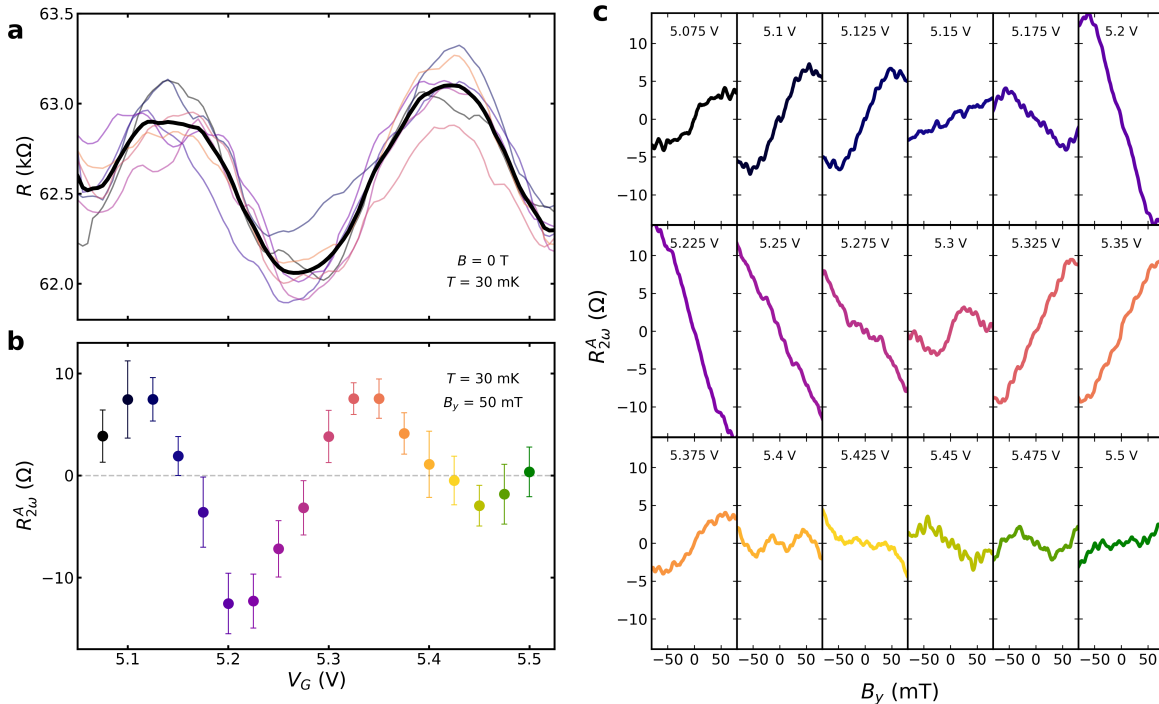


FIG. 3: **Evolution of the non-reciprocal response with changing chemical potential:** **a**, R vs V_G data of Device 3, Section 5, in a narrow range of V_G , in which the chemical potential is changed near the CNP (for a wider range of V_G , see Fig. S8a in the Supplementary Information). The peaks in R occur when the bottom of one of the quantum-confined subbands is crossed by the chemical potential; coloured thin lines show 10 individual V_G sweeps and the thick black line shows their average. **b**, $R_{2\omega}^A$ values at $B_y = 50$ mT for various gate voltages in the range corresponding to panel **a**. The zero-crossings of $R_{2\omega}^A$ roughly correspond to the peaks and dips in $R(V_G)$, and thereby are linked to the quantum-confined subbands. **c**, Averaged $R_{2\omega}^A(B_y)$ curves at various V_G settings, from which the data points in panel **b** were calculated (data points and curves are coloured correspondingly); a systematic change in the $R_{2\omega}^A(B_y)$ behaviour is clearly visible. Averages are obtained from 10 individual B -field sweeps.

METHODS

A. Theory.

Transport coefficients were calculated using the Boltzmann equation^{7,8} to attain the current density due to an electric field E up to second order such that $j = j^{(1)} + j^{(2)} = \sigma^{(1)}E + \sigma^{(2)}E^2$. As discussed in Ref. 7, experimentally the voltage drop $V = EL$ as a function of current I is measured in the form $V = R_0I(1 + \gamma BI)$. Using that $R_0 = L/\sigma^{(1)}$ for a nanowire of length L , a comparison to the experimental behaviour can then be achieved via the relation $\gamma_0 = -\frac{\sigma^{(2)}}{B(\sigma^{(1)})^2}$. Although the linear response conductivity $\sigma^{(1)}$ contains small peaks and dips due to an increased scattering rate close to the bottom of a subband, such fluctuations occur on top of a large constant conductivity and we therefore approximate $\gamma_0 \approx \frac{A}{B}\sigma^{(2)}$, with $A = -1/(\sigma^{(1)})^2$ approximately constant.

B. Material growth and device fabrication.

A 2×2 cm² thin film of $(\text{Bi}_{1-x}\text{Sb}_x)_2\text{Te}_3$ was grown on a sapphire (0001) substrate by co-evaporation of high-purity Bi, Sb, and Te in a ultra-high vacuum MBE chamber. The flux of Bi and Sb was optimized to obtain the most bulk-insulating films which was achieved with a ratio of 1:6.8. The thickness varied in the range of 14–19 nm in the whole film. Immediately after taking the film out of the MBE chamber, it was capped with a 3-nm-thick Al_2O_3 capping layer grown by atomic-layer deposition (ALD) at 80 °C using Ultratec Savannah S200. The carrier density and the mobility of the film was extracted from Hall measurements performed at 2 K using Quantum Design PPMS. Gate-tuneable multi-terminal nanowire devices were fabricated using the following top-down approach: After defining the nanowire pattern with electron-beam lithography, the film was first dry-etched using low-power Ar plasma and then wet-etched

with $\text{H}_2\text{SO}_4/\text{H}_2\text{O}_2/\text{H}_2\text{O}$ aqueous solution. To prepare contact leads, the Al_2O_3 capping layer was removed in heated Aluminum etchant (Type-D, Transene) and 5/45 nm Pt/Au contacts were deposited by UHV-sputtering. Then the whole device was capped with a 40-nm-thick Al_2O_3 dielectric grown by ALD at 80 °C, after which the 5/40nm Pt/Au top gate was sputter-deposited. Scanning electron microscopy was used to determine the exact nanowire size. The three devices reported in this paper were fabricated on the same film in one batch.

C. Second-harmonic resistance measurement.

Transport measurements were performed in a dry dilution refrigerator (Oxford Instruments TRITON 200, base temperature ~ 20 mK) equipped with a 6/1/1-T superconducting vector magnet. The first- and second-harmonic voltages were measured in a standard four-terminal configuration with a low-frequency lock-in technique at 13.37 Hz using NF Corporation LI5645. In the presence of the vector-product-type MCA with $\mathbf{P} \parallel \hat{z}$, the voltage is given by $V = R_0 I (1 + \gamma BI)$ for $\mathbf{I} \parallel \hat{x}$ and $\mathbf{B} \parallel \hat{y}$. For an ac current $I = I_0 \sin \omega t$, this becomes $V = R_0 I_0 \sin \omega t + \frac{1}{2} \gamma R_0 B I_0^2 [1 + \sin(2\omega t - \frac{\pi}{2})]$, allowing us to identify $R_{2\omega} = \frac{1}{2} \gamma R_0 B I_0$ by measuring the out-of-phase component of the ac voltage at the frequency of 2ω . The dc gate voltage was applied by using Keithley 2450.

D. Error bars.

In the plots of $R_{2\omega}^A$ vs I shown in Fig. 2c (and in Figs. S6b, S7b, and S8b of the SI), the data points for each current value are calculated by obtaining slopes from linear fits to $R_{2\omega}^A(B)$ data at that current in the indicated B -range (done individually for each measured B -sweep); the standard deviation is calculated for the set of obtained slopes at each current and used as the error bar. In the plots of $R_{2\omega}^A$ vs angle shown in Fig. 2d (and in Fig. S4 in the SI), the data points for each angle are calculated by obtaining slopes from linear fits to $R_{2\omega}^A(B)$ data at that angle in the indicated B -range (done individually for each measured B -sweep); from the set of obtained slopes at each angle, the error is calculated by using a Min-Max approach, in which we calculate the error to be half of the difference between the maximum and the minimum (calculating standard deviation gives very similar

results). In the plots of $R_{2\omega}^A$ vs V_G shown Fig. 3b, the data points for each V_G value are calculated by obtaining slopes from linear fits to $R_{2\omega}^A(B)$ data (shown in Fig. 3c) at that V_G in the indicated B -range (done individually for each measured B -sweep); from the set of obtained slopes per V_G , the standard deviation is calculated and used as the error bar.

Acknowledgements: We acknowledge useful discussions with A. Rosch and B. Shklovskii. This work was supported by the Georg H. Endress Foundation, the Swiss National Science Foundation, and NCCR QSIT. This project has received funding from the European Research Council (ERC) under the European Union’s Horizon 2020 research and innovation programme (grant agreement No 741121 and grant agreement No 757725). It was also funded by the Deutsche Forschungsgemeinschaft (DFG, German Research Foundation) under CRC 1238 - 277146847 (Subprojects A04 and B01) as well as under Germany’s Excellence Strategy - Cluster of Excellence Matter and Light for Quantum Computing (ML4Q) EXC 2004/1 - 390534769. G.L. acknowledges the support by the KU Leuven BOF and Research Foundation Flanders (FWO, Belgium), file No. 27531 and No. 52751.

Author contributions: H.F.L. with help from J.K., D.L., and Y.A. conceived the project. H.F.L. with help from J.K. and D.L. performed the theoretical calculations. M.R. fabricated the devices, performed the experiments and analysed the data with help from H.F.L, F.M., D.F., O.B, and Y.A. A.B., G.L, A.U. and A.T. provided the material. H.F.L., M.R., D.L., J.K., and Y.A. wrote the manuscript with inputs from all authors.

Competing interests: The authors declare no competing interests.

Correspondence: Correspondence and requests for materials should be addressed to H.F.L. (henry.legg@unibas.ch), J.K. (jelena.klinovaja@unibas.ch), or Y.A. (ando@ph2.uni-koeln.de).

Data availability: The data that support the findings of this study are available from the corresponding author upon reasonable request.

-
- [1] Ando, F. *et al.* Observation of superconducting diode effect. *Nature* **584**, 373–376 (2020).
 [2] Isobe, H., Xu, S.-Y. & Fu, L. High-frequency rectification via chiral Bloch electrons. *Sci. Adv.* **6**, eaay2497 (2020).
 [3] Rikken, G. L. J. A., Fölling, J. & Wyder, P. Electrical

magneto-chiral anisotropy. *Phys. Rev. Lett.* **87**, 236602 (2001).

- [4] Rikken, G. L. J. A. & Wyder, P. Magnetoelectric anisotropy in diffusive transport. *Phys. Rev. Lett.* **94**, 016601 (2005).

- [5] Tokura, Y. & Nagaosa, N. Nonreciprocal responses from non-centrosymmetric quantum materials. *Nat. Commun.* **9**, 3740 (2018).
- [6] Morimoto, T. & Nagaosa, N. Chiral anomaly and giant magnetochiral anisotropy in noncentrosymmetric Weyl semimetals. *Phys. Rev. Lett.* **117**, 146603 (2016).
- [7] Ideue, T. *et al.* Bulk rectification effect in a polar semiconductor. *Nat. Phys.* **13**, 578–583 (2017).
- [8] Wang, Y. *et al.* Gigantic magnetochiral anisotropy in the topological semimetal ZrTe₅. *arXiv:2011.03329* (2020).
- [9] Legg, H. F., Loss, D. & Klinovaja, J. Majorana bound states in topological insulators without a vortex. *arXiv preprint arXiv:2103.13412* (2021).
- [10] Krstić, V., Roth, S., Burghard, M., Kern, K. & Rikken, G. Magneto-chiral anisotropy in charge transport through single-walled carbon nanotubes. *J. Chem. Phys.* **117**, 11315–11319 (2002).
- [11] Zhang, Y. & Vishwanath, A. Anomalous Aharonov-Bohm conductance oscillations from topological insulator surface states. *Phys. Rev. Lett.* **105**, 206601 (2010).
- [12] Ziegler, J. *et al.* Probing spin helical surface states in topological HgTe nanowires. *Phys. Rev. B* **97**, 035157 (2018).
- [13] de Juan, F., Bardarson, J. H. & Ilan, R. Conditions for fully gapped topological superconductivity in topological insulator nanowires. *SciPost Phys.* **6**, 60 (2019).
- [14] Munning, F. *et al.* Quantum confinement of the Dirac surface states in topological-insulator nanowires. *Nat. Commun.* **12**, 1–6 (2021).
- [15] Breunig, O. & Ando, Y. Opportunities in topological insulator devices. *arXiv preprint arXiv:2101.12538* (2021).
- [16] Štréda, P. & Šeba, P. Antisymmetric spin filtering in one-dimensional electron systems with uniform spin-orbit coupling. *Phys. Rev. Lett.* **90**, 256601 (2003).
- [17] Braunecker, B., Japaridze, G. I., Klinovaja, J. & Loss, D. Spin-selective Peierls transition in interacting one-dimensional conductors with spin-orbit interaction. *Phys. Rev. B* **82**, 045127 (2010).

Supplementary Information for:
Giant magnetochiral anisotropy from quantum confined surface states
of topological insulator nanowires

Henry F. Legg,^{1,*} Matthias Röbner,^{2,*} Felix Münnig,² Dingxun Fan,²
Oliver Breunig,² Andrea Bliesener,² Gertjan Lippertz,^{2,3} Anjana Uday,²
A. A. Taskin,² Daniel Loss,¹ Jelena Klinovaja,¹ and Yoichi Ando²

¹*Department of Physics, University of Basel,
Klingelbergstrasse 82, CH-4056 Basel, Switzerland*

²*Physics Institute II, University of Cologne,
Zùlpicher Str. 77, 50937 Köln, Germany*

³*KU Leuven, Quantum Solid State Physics,
Celestijnenlaan 200 D, 3001 Leuven, Belgium*

* These authors contributed equally

S1. THEORETICAL DESCRIPTIONS

A. Band structure and influence of gating

The surface states of a TI nanowire are quantum confined such that the states have half-integer angular momentum $\ell = \pm\frac{1}{2}, \frac{3}{2}, \dots$ around the nanowire and obey the dispersion relation [1]

$$\epsilon_\ell(k) = \pm v_F \sqrt{k^2 + (\ell/r)^2}, \quad (1)$$

where k is the momentum along the nanowire, $2\pi r$ is the nanowire perimeter, and v_F is the Fermi velocity. Application of a gate voltage, for instance, from the top of the TI nanowire, induces a non-uniform chemical potential $\mu(\phi) = \mu + \delta\mu(\phi)$ in the nanowire cross-section [1–3], where μ is the chemical potential on the nanowire surface (measured from the Dirac point) and $\phi = 0$ is the angle from the direction normal to the gate. The non-uniformity of chemical potential breaks inversion symmetry and can result in a large spin-splitting of the subbands for finite momentum k along the nanowire (see Fig. 1c main text). For an idealised circular nanowire and non-uniformities smaller than the subband gap – although also valid for larger non-uniformities – it has been shown that the dispersion is given by (see Ref. 3 for details)

$$\varepsilon_\ell^\pm(k) \approx \epsilon_\ell(k) \pm \frac{k\mu_{2\ell}}{\sqrt{k^2 + (\ell/r)^2}}, \quad (2)$$

and similarly $-\varepsilon_\ell^\pm(k)$ below the Dirac point. Here the bands are labelled by $\ell > 0$ and μ_n is the n th Fourier coefficient of the non-uniform chemical potential $\delta\mu(\phi) = \sum_n \mu_n \cos n\phi$ assuming the potential is symmetric for $\pm\phi$. The magnitude of the splitting does not depend strongly on the exact shape of the potential, $\delta\mu(\phi)$, other than through the components μ_n [3]. The band splitting due to such a non-uniform potential is shown in Fig. 1c in the main text.

When inversion symmetry is broken by a non-uniform chemical potential the states in the split-bands possess a finite spin polarisation in the y -direction [3]. As a result, as discussed in the main text, when a magnetic field is applied parallel to this direction the bands shift relative to each other by the Zeeman energy $\pm g\mu_B B_y/2$ with g the effective g -factor of the split subband and μ_B is the Bohr magneton. The situation can be modelled analytically by considering helical bands – valid in the limit of small non-uniformities – such that the subbands $\varepsilon_\ell^\pm(k)$ above the Dirac point are given by

$$\varepsilon_\ell^\pm(k) \approx \epsilon_\ell(k) \pm \frac{k\mu_{2\ell}}{\sqrt{k^2 + (\ell/r)^2}} \pm \frac{g\mu_B B_y}{2} \quad (3)$$

and similarly $-\varepsilon_\ell^\pm(k)$ below the Dirac point (see Fig. 1c main text). We note that orbital effects for magnetic field B_x along the wire should open a gap in the dispersion [3]. However, for the small $B = 110$ mT field used in the experimental angular rotation α the size of such a gap will be very small – since this field strength is considerably less than a flux quantum corresponding to a field value $B \sim 1.4$ T for the given nanowire cross-section – as such orbital effects will only alter the MCA for a very small range of chemical potentials and only for $\alpha \sim 90^\circ$ or $\alpha \sim 270^\circ$ in Fig. 2d

of the experiment. We therefore neglect orbital effects in our theoretical analysis and focus on the influence of the Zeeman terms due to a magnetic field $\mathbf{B} \parallel \hat{\mathbf{y}}$.

B. Linear and second order response conductivity from the Boltzmann equation

Since the gate and magnetic field break inversion and time-reversal symmetry, respectively, an MCA is symmetry allowed for the setup shown in Fig. 1b. In this section, we use the Boltzmann equation in the relaxation time approximation to derive the conductivity expanded to linear and second order in electric field, i.e. the linear and second order conductivity [4, 5]. This approach is valid in the diffusive limit, relevant for the bulk-insulating TI nanowires in our experiment [1]. We start by considering a scattering time which is independent of the chemical potential $\tau(\mu) = \tau$. Later in this section we will consider the influence of broadening processes such as Coulomb disorder and the inclusion of the dependence of scattering time on chemical potential.

Boltzmann equation for 1st order conductivity: We begin by expanding the distribution function of states in a given subband labelled by (ℓ, \pm) as $f^{\pm, \ell} = f_0^{\pm, \ell} + f_1^{\pm, \ell} + f_2^{\pm, \ell} + \dots$, where $f_n^{\pm, \ell}$ is the n th order response to an electric field E of the \pm branch of ℓ th subband [4]. The distribution function to first order in E within the relaxation time approximation of the Boltzmann equation is therefore given by

$$f_1^{\pm, \ell} \approx \frac{e\tau E}{\hbar} \frac{\partial f_0^{\pm, \ell}}{\partial k} = e\tau E v_\ell^\pm(k) \frac{\partial f_0^{\pm, \ell}}{\partial \varepsilon_\ell^\pm(k)}, \quad (4)$$

where $v_\ell^\pm(k) = \frac{1}{\hbar} \partial_k \varepsilon_\ell^\pm(k)$ is the velocity and e the elementary charge. We use the Fermi-Dirac distribution function for $f_0^{\pm, \ell} = f_0(\varepsilon_\ell^\pm(k) - \mu)$.

Next, we calculate the current density $j = j^{(1)} + j^{(2)} + \dots$ expanded order by order in electric field. We begin by utilising the first order distribution function to calculate the current density $j^{(1)}$ which is first order in electric field E (with coefficient given by the linear response conductivity $\sigma^{(1)}$) such that

$$\begin{aligned} j^{(1)} &\equiv E\sigma^{(1)} = -e \sum_{\eta=\pm} \sum_{\ell=\frac{1}{2}, \frac{3}{2}, \dots} \int \frac{dk}{2\pi} v_\ell^\eta(k) f_1^{\eta, \ell} \\ &= e^2 E \sum_{\eta=\pm} \sum_{\ell=\frac{1}{2}, \frac{3}{2}, \dots} \tau \int \frac{dk}{2\pi} [v_\ell^\eta(k)]^2 \delta(\mu - \varepsilon_\ell^\eta(k)) \\ &= \frac{e^2}{h} E \sum_{\eta=\pm} \sum_{\ell=\frac{1}{2}, \frac{3}{2}, \dots} \tau [v_\ell^\eta(k_{\ell, R}^\eta) - v_\ell^\eta(k_{\ell, L}^\eta)], \end{aligned} \quad (5)$$

where in the second line we used that the Fermi-Dirac distribution at zero temperature is given by $\frac{\partial f_0^{\pm, \ell}}{\partial \varepsilon_\ell^\pm(k)} = -\delta(\mu - \varepsilon_\ell^\pm(k))$ and, as in the main text, $k_{\ell, R}^\eta$ and $k_{\ell, L}^\eta$ are right and left Fermi wave vectors for the $\eta = \pm$ branch of ℓ th subband (see Fig. 1c main text). In general, these wave vectors $k_{\ell, L/R}^\eta$ can be found by numerically solving the equation $\varepsilon_\ell^\eta(k_{\ell, L/R}^\eta) = \mu$. Note that if the band is not occupied then it will not contribute to the current density j . Finally, we also note that setting

magnetic field to zero ($B = 0$) and non-uniform chemical potential to zero ($\delta\mu(\phi) = 0$) we find that $\sigma^{(1)}(\mu)$ coincides with the result with the same limit in Ref. [1] derived from the Kubo formula.

Boltzmann equation for 2nd order conductivity: The E^2 contribution to the current density $j^{(2)}$ can be obtained similarly by using the first order of the distribution function $f_1^{\pm,\ell}$ from above such that in the relaxation time approximation [4] we arrive at

$$f_2^{\pm,\ell} \approx \frac{e\tau E}{\hbar} \frac{\partial f_1^{\pm,\ell}}{\partial k} = \left(\frac{e\tau E}{\hbar} \right)^2 \frac{\partial^2 f_0^{\pm,\ell}}{\partial k^2}. \quad (6)$$

Inserting this expression for $f_2^{\pm,\ell}$ into the Boltzmann equation gives the component of current density proportional to the square of the electric field as

$$\begin{aligned} j^{(2)} &\equiv \sigma^{(2)} E^2 = -e \sum_{\eta=\pm} \sum_{\ell=\frac{1}{2}, \frac{3}{2}, \dots} \int \frac{dk}{2\pi} v_\ell^\eta(k) f_2^{\eta,\ell} = -e \left(\frac{e\tau E}{\hbar} \right)^2 \sum_{\eta=\pm} \sum_{\ell=\frac{1}{2}, \frac{3}{2}, \dots} \int \frac{dk}{2\pi} v_\ell^\eta(k) \frac{\partial^2 f_0^{\pm,\ell}}{\partial k^2} \quad (7) \\ &= -e \left(\frac{e\tau E}{\hbar} \right)^2 \sum_{\eta=\pm} \sum_{\ell=\frac{1}{2}, \frac{3}{2}, \dots} \int \frac{dk}{2\pi} v_\ell^\eta(k) \frac{\partial^2 \varepsilon_k^\eta}{\partial k^2} \delta(\mu - \varepsilon_k^\eta) \\ &= -\frac{e^3}{\hbar} E^2 \sum_{\eta=\pm} \sum_{\ell=\frac{1}{2}, \frac{3}{2}, \dots} \tau^2 [\mathcal{V}_\ell^\eta(k_{\ell,R}^\eta) - \mathcal{V}_\ell^\eta(k_{\ell,L}^\eta)], \end{aligned}$$

where $\mathcal{V}_\ell^\pm(k) = \frac{1}{\hbar^2} \partial_k^2 \varepsilon_\ell^\pm(k)$ denotes the band curvature and the second line requires integration by parts. We use this to acquire the MCA rectification coefficient

$$\gamma = \frac{-\sigma^{(2)}}{B(\sigma^{(1)})^2} = \sum_{\ell=\frac{1}{2}, \frac{3}{2}, \dots} \gamma_\ell, \quad (8)$$

with γ_ℓ given by Eq. (1) of the main text. We note that for a purely parabolic band, for example, in a Rashba nanowire where to good approximation $\varepsilon_\pm(k) = (k \pm k_{\text{so}})^2/2m$, the quantity $\mathcal{V}_\ell^\pm(k) = 1/m$ is independent of the Fermi wavevectors $k_{L/R}^\pm$ if the magnetic field points along the spin-orbit interaction vector and, thus, the two contributions γ_ℓ^\pm of Eq. (1) in the main text would cancel each other. Hence, the giant size of the MCA is a unique feature of the peculiar dispersion of TI subbands. In what follows we focus on the contribution of an individual subband pair via γ_ℓ . We note that the precise magnitude of the harmonics μ_n depends on several experimental factors which are difficult to model theoretically, these include the electrostatics of the nanowire setup, screening effects (e.g. from contacts), and the exact geometry of the nanowires. Using Eq. (7) and the eigenenergies from Eq. (3) gives the result shown in Fig. 1d of the main text. Finally, we note that $\sigma^{(2)}$ is zero when the chemical potential is uniform in the cross-section (i.e. $\mu_n = 0$ for all n) or when the magnetic field is absent (i.e. $g\mu_B B_y/2 = 0$). In other words there is only a finite MCA when *both* inversion symmetry and time reversal symmetry are broken simultaneously, as expected.

Estimate of rectification effect: To obtain a theoretical estimate of the size of the maximum

possible MCA rectification γ in a typical nanowire we first use the experimental fact that the Ohmic resistance of a $L \sim 5 \mu\text{m}$ nanowire (e.g. the resistance of Device 3, Section 5 (see Fig. S8a) saturates at $R \sim 60 \text{ k}\Omega$ as function of gate voltage with only small fluctuations around this value, these oscillation can be attributed to the quantum confinement of surface states. For the $w \approx 200 \text{ nm}$ and $h \approx 16 \text{ nm}$ nanowires used in our experiment the presence of these fluctuations suggests that the broadening due to disorder is smaller than the subband spacing, i.e. $\tau \gtrsim \hbar/(1 \text{ meV}) \sim 1 \text{ ps}$, in fact this value also fits well with the $\sigma^{(1)} \sim 0.1 \mu\text{m}/\text{k}\Omega$ found experimentally. Numerically calculating $\sigma^{(2)}(\mu)$ using Eq. (7) we find that the maximum $|\sigma^{(2)}| \sim e^3(\tau/\hbar)^2(2500 \text{ meV nm}^2)/h$ close to the bottom of the subband pair, here we use the small angular momenta $\ell = 3/2$, Fourier coefficient $\mu_{2\ell} \sim \ell v/r$, $v \sim 5 \times 10^5 \text{ m/s}$, and $B \sim 0.05 \text{ T}$ with the g -factor $g \approx 4$ [6]. Therefore, we estimate the order of magnitude for the maximal rectification γ_ℓ from a given subband pair as

$$|\gamma_\ell^{\text{max}}| = \frac{|\sigma^{(2)}|}{B(\sigma^{(1)})^2} \sim \frac{e^3(1 \text{ ps}/\hbar)^2(2500 \text{ meV nm}^2)}{h(0.05 \text{ T})(0.1 \mu\text{m}/\text{k}\Omega)^2} \sim 5 \times 10^5 \text{ A}^{-1}\text{T}^{-1}. \quad (9)$$

This estimate represents only an approximation of the order of magnitude that one can expect due to MCA in TI nanowires, showing that it is extremely large. In real experimental systems the value of $|\gamma_\ell^{\text{max}}|$ could even be larger if the non-uniformity of chemical potential across the nanowire cross-section, characterised by the Fourier harmonics μ_n , is larger than assumed here. It is, however, as found in experiment, more likely that $|\gamma_\ell^{\text{max}}|$ is reduced in size by several factors such as the chemical potential dependence of scattering time, smearing of chemical potential due to Coulomb disorder, and further effects not considered in this simple approximation, for instance the separate contributions of bulk and surface conductivity channels. Note that throughout the calculations above, there is an assumption that $|E\sigma^{(2)}| \ll |\sigma^{(1)}|$ is always satisfied; when this assumption is not satisfied, our second-order theory breaks down. Although the rectification is giant in comparison to the largest γ values observed so far, the estimate given in Eq. (9) is still orders of magnitude below this bound for all values of B and I in our experiment.

Influence of Coulomb disorder: One reasons for the lower experimental value than the estimate of Eq. (9) is the influence of Coulomb disorder in the bulk and on the surface of the TI nanowire [7–10]. In general, such Coulomb disorder leads to fluctuations in the local chemical potential of the nanowire surface, resulting in so-called surface puddles. These surface puddles smear out the chemical potential and lead to an averaging of γ_ℓ over the length of the nanowire [10]. To approximate the influence of such surface puddles we use our result from Eq. (7) and assume that the surface fluctuations of chemical potential belong to a Gaussian distribution of width Γ , such that

$$\bar{\gamma}_\ell(\mu) = \frac{1}{\Gamma\sqrt{2\pi}} \int_{-\infty}^{\infty} d\mu' \gamma_\ell(\mu') e^{-\frac{1}{2}\left(\frac{\mu-\mu'}{\Gamma}\right)^2}. \quad (10)$$

We show $\bar{\gamma}_\ell(\mu)$ for several distributions widths Γ in Fig. S1. As expected, for not unrealistic broadenings Γ , the smearing results in a smoothing of the function $\gamma_\ell(\mu)$ and a reduction in the maximum possible rectification $|\bar{\gamma}_\ell^{\text{max}}|$. The density of Coulomb disorder and its influence on the surface states of TI nanowires remains an open experimental question, but the presence of quantum confinement oscillations in the resistivity curves suggests that the broadening Γ of our

ribbon-shaped experimental nanowires is smaller than or similar to the subband spacing.

Influence of scattering time: In the experiment, quantum confinement features in the Ohmic resistance R due to increased scattering near the bottom of subbands are weak ($\sim 5\%$ of the total R , see Fig. 3a), and so, to a good approximation, τ can be taken as constant (as above). In theory, for a nanowire with perfect quantum confinement and only surface contributions to the conductivity, the scattering time τ becomes very strongly dependent on the position of the chemical potential within a given subband due to the divergence in density of states at subband minima in one dimension [1]. For completeness, here we take the opposite limit and assume the scattering time is strongly dependent on chemical potential and consider how this would affect $\sigma^{(2)}(\mu)$ and hence $\gamma_\ell(\mu)$. We will see that the overall qualitative features of $\gamma_\ell(\mu)$ are largely unchanged in this limit.

To estimate the scattering time we will use the Born approximation [1] valid for weak impurity scattering potential u_0 and low impurity density n_{imp} and assume that spin-flip interband scattering

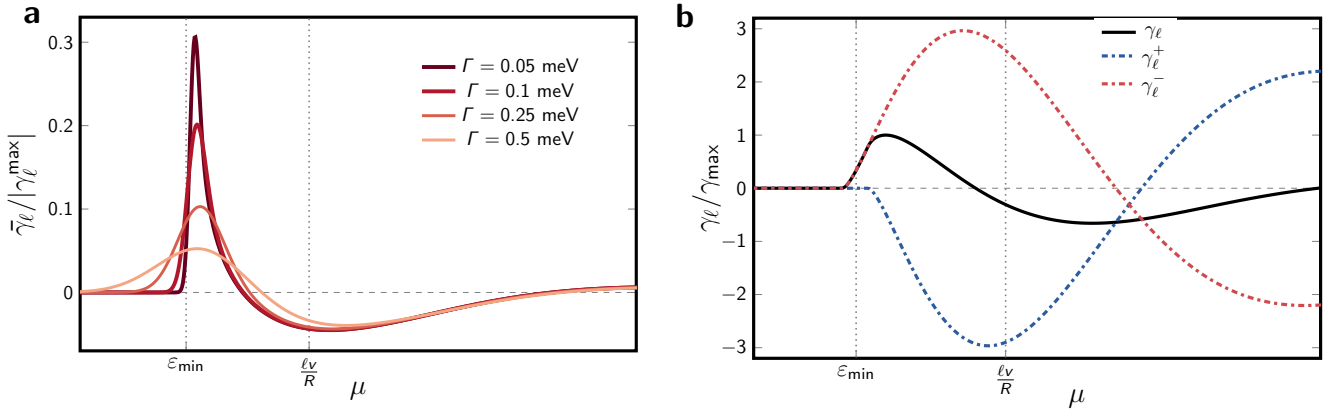


FIG. S1: **Influence of different disorder effects:** **a**, Influence of Coulomb disorder: Charged impurities in the bulk and on the surface of the TI smear out the chemical potential μ which leads to a reduction and smoothing of γ_ℓ , here shown for a constant scattering time τ . We choose realistic experimental parameters $B = 0.05$ T, $g = 4$, $v_F = 5 \times 10^5$ m/s, $\tau \sim 1$ ps. For this plot we also chose $\ell = 3/2$ with the Fourier harmonic $\mu_{2\ell} \approx v_F \ell / r \approx 3.9$ meV. This gives $|\gamma_\ell^{\max}| \sim 5 \times 10^5$ T $^{-1}$ A $^{-1}$ as discussed in the text. These are the same parameters as in Fig. 1d of the main text, apart from there $B = 1$ T is used for clarity of the different contributions. **b**, Influence of strong subband minimum scattering: Although only weakly visible in our experimental devices, close to a given subband minimum there is an increase in the scattering rate $1/\tau$ due to the diverging density of states [1]. Here, we show that, even in nanowires in which τ is very strongly dependent on chemical potential μ (such that $\tau = 0$ at the bottom of the band), the overall qualitative features of γ_ℓ will be largely unaffected by such a divergence, with a pronounced maximum and change in sign still clearly visible. We use the same parameters as in **a**, apart from $B = 1$ T for clarity of the different contributions. For simplicity in this plot we assume $\sigma^{(1)} \approx \text{const.}$ since there are more conductivity channels for Ohmic conductivity, i.e. through the bulk. In reality $\sigma^{(1)}$ will also inherit the additional dependence on τ which will lead to an increase in γ_ℓ close to ϵ_{\min} .

is negligible. The scattering time for the separate \pm bands at zero temperature is given by

$$\frac{\hbar}{\tau^\pm(\mu)} \approx n_{\text{imp}} u_0^2 \sum_{\ell=\frac{1}{2}, \frac{3}{2}, \dots} \int \frac{dk}{2\pi} \delta(\mu - \varepsilon_\ell^\pm(k)) = n_{\text{imp}} u_0^2 \sum_{\ell=\frac{1}{2}, \frac{3}{2}, \dots} \rho_\ell^\pm(\mu), \quad (11)$$

where

$$\rho^\pm(\mu) = \sum_{\ell=\frac{1}{2}, \frac{3}{2}, \dots} \left(\frac{1}{\hbar |v_\ell^\pm(k_{\ell,L}^\pm)|} + \frac{1}{\hbar |v_\ell^\pm(k_{\ell,R}^\pm)|} \right) \quad (12)$$

is the density of states of the respective \pm bands. The linear response and second harmonic conductivities are obtained with the replacement $\tau \rightarrow \tau^\pm(\mu)$. The density of states in Eq. (12) diverges at the bottom of a given subband leading to a rapid increase in the scattering rate at this point [1], however, the qualitative features of $\sigma^{(2)}(\mu)$ and hence γ_ℓ within a given subband are not strongly modified by this additional dependence of $\tau(\mu)$ (see Fig. S1b). Additionally, the divergence of scattering rate will be cut-off by temperature and disorder, we can therefore expect that the true experimental behaviour of γ_ℓ is somewhere between the two scenarios shown in Fig. S1b and Fig. 1d of the main text.

S2. EXPERIMENTAL DESCRIPTIONS

A. Materials characterization

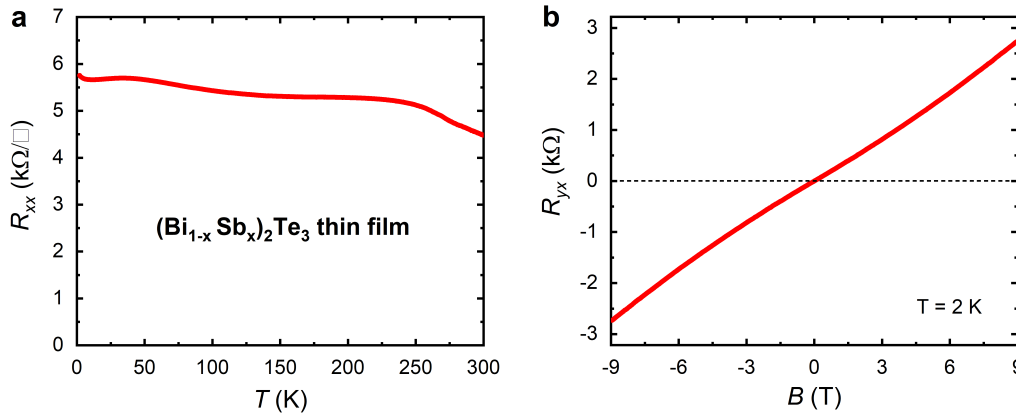


FIG. S2: **Transport properties of the $(\text{Bi}_{1-x}\text{Sb}_x)_2\text{Te}_3$ thin film used for the nanowire device fabrication.** **a**, Temperature dependence of the sheet resistance R_{xx} of the thin film used in this study. A six-terminal measurement was done on a small part of the $2 \times 2 \text{ cm}^2$ film. **b**, Magnetic-field dependence of the Hall resistance R_{yx} at 2 K.

Figure S2 shows the the temperature dependence of the sheet resistance R_{xx} and the magnetic-field dependence of the Hall resistance R_{yx} measured on a small piece taken from the $(\text{Bi}_{1-x}\text{Sb}_x)_2\text{Te}_3$ (BST) thin film that was used for fabricating all the nanowire devices. The $R_{xx}(T)$ behavior is

typical for a bulk-insulating BST thin film, which is corroborated by the low 2D hole carrier density of only $n \sim 1.8 \times 10^{12} \text{ cm}^{-2}$ calculated from dR_{yx}/dB at $B = 0 \text{ T}$. We also obtain the mobility $\mu \simeq 600 \text{ cm}^2/\text{Vs}$ from the data in Fig. S2.

B. Raw data of $R_{2\omega}$ and symmetric component

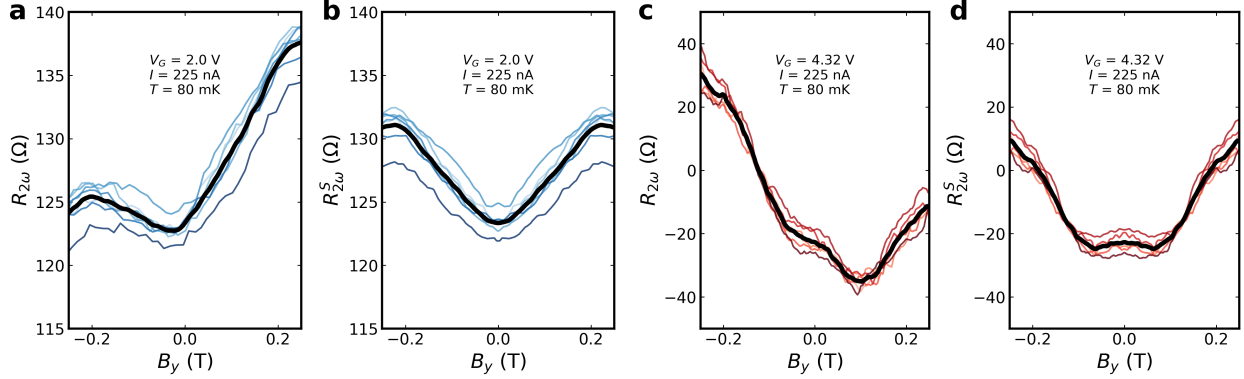


FIG. S3: **Raw $R_{2\omega}$ data and symmetric component $R_{2\omega}^S$ of Device 1, Section 1.** **a**, Raw $R_{2\omega}$ vs B_y data at $V_G = 2 \text{ V}$. **b**, The symmetric component $R_{2\omega}^S$ extracted from the raw data for $V_G = 2 \text{ V}$. **c**, Analogously, raw $R_{2\omega}$ vs B_y data at $V_G = 4.32 \text{ V}$. **d**, The symmetric component $R_{2\omega}^S$ extracted from the raw data for 4.32 V . The corresponding extracted asymmetric components $R_{2\omega}^A$ are shown in Fig. 2b of the main text. Coloured thin lines show the results of 7 sweeps, and the thick black line shows their average.

Upon sweeping the magnetic field B_y applied perpendicular to both the current I and the gate-induced electric field E , the second-harmonic voltage $R_{2\omega}$ comprises an antisymmetric component $R_{2\omega}^A$ and a symmetric component $R_{2\omega}^S$; these two components can be easily separated by antisymmetrization/symmetrization of the B -dependence data. Figures S3a and S3c show the raw $R_{2\omega}$ data for $V_G = 2 \text{ V}$ and 4.32 V , respectively, from which the $R_{2\omega}^A$ data shown in Fig. 2b of the main text were extracted. The $R_{2\omega}^S$ component shown in Figs. S3b and S3d can have various trivial origins such as a diode-like effect at an imperfect contact.

C. Magnetic-field-orientation dependence of γ for the out-of-plane rotation

In addition to the magnetic-field-orientation dependence of $R_{2\omega}^A$ for the in-plane rotation shown in the main text (Fig. 2d), we have taken similar data for the out-of-plane rotation (Fig. S4) and found that the behaviour is consistent with the $\gamma \approx \gamma_0 \cos \beta$ dependence, where β is the angle of the B -field away from the y -direction in the yz -plane. Each data point was generated by averaging 6 (8) individual B -field sweeps for 2 V (4.32 V), while the error was calculated by a Min-Max method (though a standard deviation approach gives very similar results). We note that the γ_0 values for the in-plane and out-of-plane rotations at nominally the same V_G are slightly different;

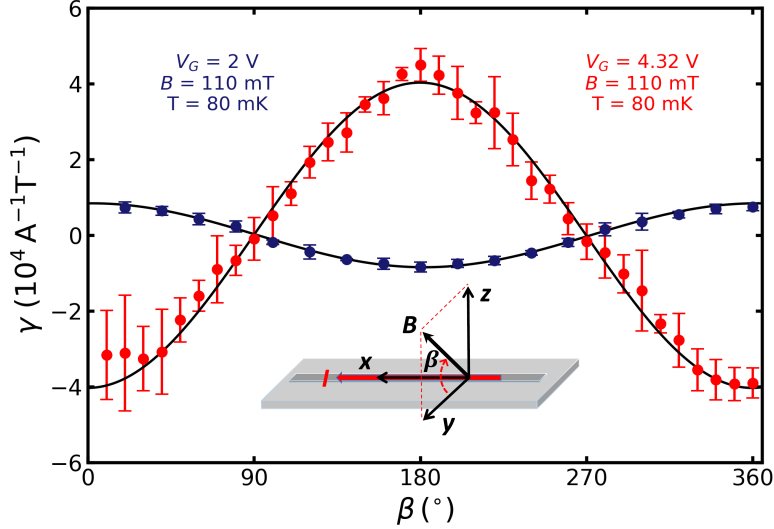


FIG. S4: **Magnetic-field-orientation dependence of γ for the out-of-plane rotation in Device 1, Section 1. a**, When the B -field is rotated in the yz -plane, the MCA coefficient γ obeys $\gamma \approx \gamma_0 \cos \beta$, where β is the angle from the y -direction. The data shown here is for Device 1, Section 1, at V_G of 2 V (blue) and 4.32 V (red). Solid black lines are fits to the expected cosine dependence. The inset shows the definition of β and the coordinate system.

this is probably due to a difference in the details of the charge distributions and a slightly different chemical potentials for the two measurements, since the gating history was different.

D. Reproducibility of the magnetochiral anisotropy

To confirm the reproducibility of the experimental data supporting a giant MCA in BST nanowires, additional measurements have been performed on three different devices (Device 1, 2, 3) at various nanowire sections. All three devices had the same design (with slightly different width) and were fabricated from the same thin film in the same fabrication batch. The nanowire width was ~ 200 , ~ 205 , and ~ 210 nm in Device 1, 2, and 3, respectively, with the film thickness of ~ 16 nm. In the following, we show representative data reconfirming the behaviours reported in the main text.

Figure S5 shows a data set to confirm the sign change in γ upon a slight change in the chemical potential. The data were taken on Section 1 of Device 1.

Figures S6 and S7 show further data, taken on Section 2 of Device 1 and Section 1 of Device 2, respectively, to demonstrate that our BST nanowires consistently show the large MCA. The three basic characteristics of the vector-product-type MCA are: (i) $R_{2\omega}^A$ depends linearly on B at low field, (ii) $R_{2\omega}^A$ is maximum for $\mathbf{B} \parallel \hat{\mathbf{y}}$ and vanishes for $\mathbf{B} \parallel \mathbf{I}$, and (iii) $R_{2\omega}^A$ increases linearly with I . All three characteristics are reproduced.

Figure S8 shows supplemental data for Device 3 which was used for demonstrating the repeated sign change in γ as a function of V_G in the main text. The V_G dependence of R is shown in

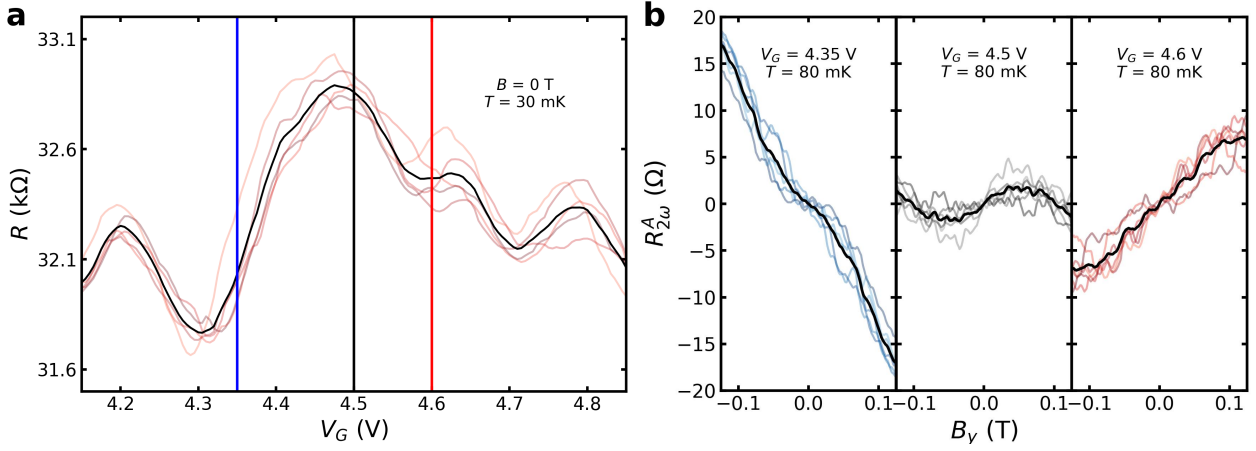


FIG. S5: **Sign change of γ upon changing the chemical potential in Device 1, Section 1.** **a**, The V_G -dependence of R in the V_G range of 4.15–4.9 V obtained in a different sweep from that in Fig. 2a of the main text. Thin coloured lines are the data from 5 individual V_G sweeps and the thick black line is their average. The blue, black, and red vertical lines mark the V_G values at which the B -dependence of $R_{2\omega}^A$ was measured. **b**, Plots of $R_{2\omega}^A$ vs B_y at the V_G values of 4.35 V, 4.5 V, and 4.6 V, which span a peak in the $R(V_G)$ curve shown in panel **a**. The sign of $dR_{2\omega}^A/dB_y$ near $B_y = 0$ T (i.e. the sign of γ) changes in this V_G interval. Coloured thin lines show 6 individual B -field sweeps and the thick black line shows their average.

Fig. S8a for a wide range of V_G . The I -linear increase of $R_{2\omega}^A$ is shown in Fig. S8b. The B -linear dependence of $R_{2\omega}^A$ for $\mathbf{B} \parallel \hat{\mathbf{y}}$ and vanishing $R_{2\omega}^A$ for $\mathbf{B} \parallel \mathbf{I}$ are shown for both positive and negative γ in Figs. S8c and S8d, respectively.

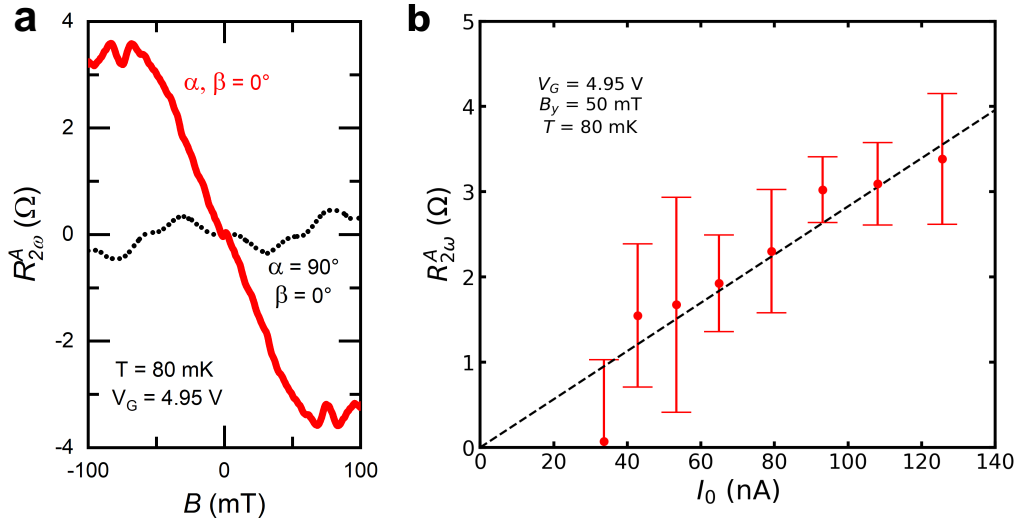


FIG. S6: **MCA in Device 1, Section 2.** **a**, Averaged $R_{2\omega}^A(B)$ behaviours for $\mathbf{B} \parallel \hat{y}$ (red solid line) and $\mathbf{B} \parallel \mathbf{I}$ (black dotted line) at $V_G = 4.95$ V measured on Section 2 of Device 1. Averages are obtained from 10 individual B -field sweeps. **b**, $R_{2\omega}^A$ at $V_G = 4.95$ V as a function of the ac excitation current I_0 for $B_y = 50$ mT. The black dashed line is a guide to the eye to mark the linear behaviour.

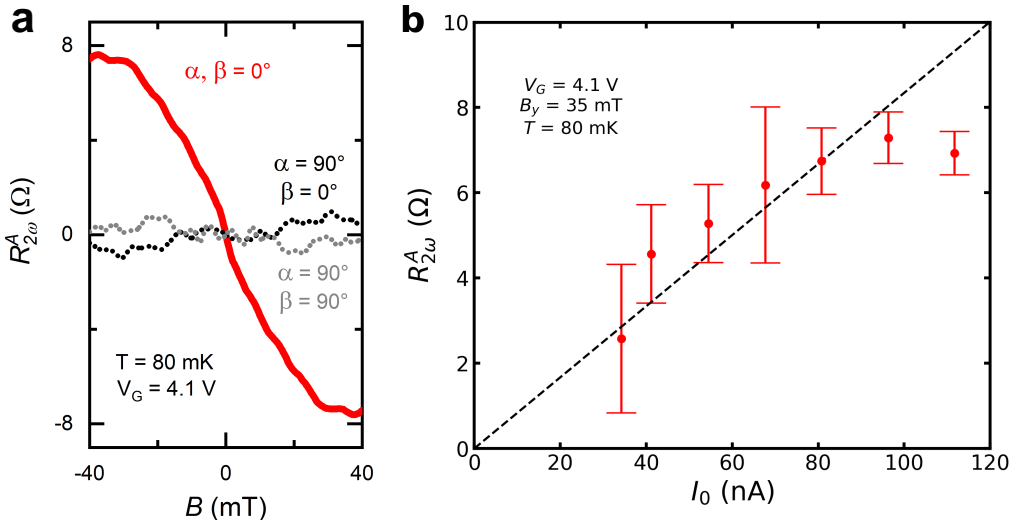


FIG. S7: **MCA in Device 2, Section 3.** **a**, Averaged $R_{2\omega}^A(B)$ behaviours for $\mathbf{B} \parallel \hat{y}$ (red solid line), $\mathbf{B} \parallel \mathbf{I}$ (black dotted line) and $\mathbf{B} \parallel \hat{z}$ (grey dotted line) at $V_G = 4.1$ V measured on Section 3 of Device 2. Averages are obtained from 10 individual B -field sweeps. **b**, $R_{2\omega}^A$ at $V_G = 4.1$ V as a function of the ac excitation current I_0 for $B_y = 30$ mT. The black dashed line is a guide to the eye to mark the linear behaviour.

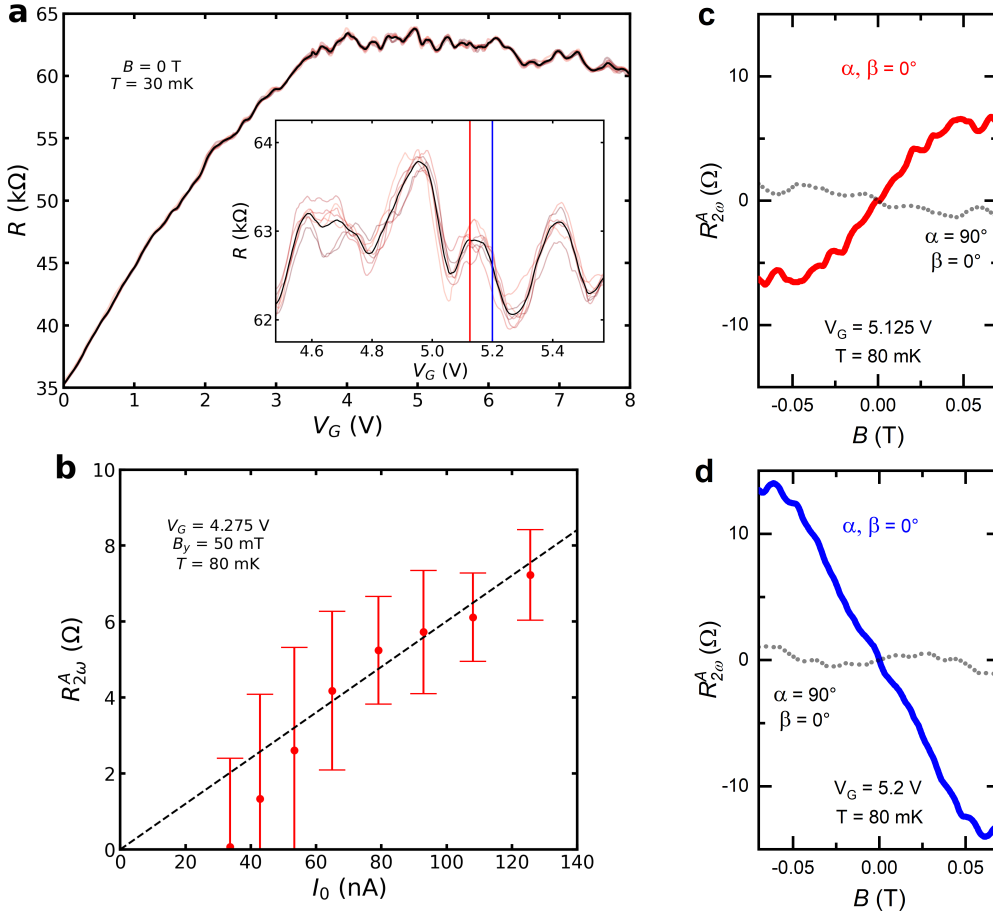


FIG. S8: **MCA in Device 3, Section 5.** **a**, $R(V_G)$ behaviour of the Section 5 of Device 3 in a wide V_G range, presenting a broad maximum around $V_G \simeq 5$ V. Coloured thin lines show 7 uni-directional V_G sweeps and the thick black line shows the average. Inset shows a magnification of the V_G range 4.5–5.6 V; the red and blue vertical lines mark the V_G positions used for the $R_{2\omega}^A(B)$ measurements shown in panels **c** and **d**. **b**, $R_{2\omega}^A$ at $V_G = 4.275$ V as a function of the ac excitation current amplitude I_0 for $B = 50$ mT applied along \hat{y} . The black dashed line is a guide to the eye. **c,d** Averaged $R_{2\omega}^A(B)$ behaviours for $\mathbf{B} \parallel \hat{y}$ (solid lines) and $\mathbf{B} \parallel \mathbf{I}$ (dotted lines) at $V_G = 5.125$ V (**c**) and 5.2 V (**d**). The sign of $dR_{2\omega}^A/dB_y$ near $B = 0$ T (i.e. the sign of γ) changes in this narrow V_G interval crossing a peak in the $R(V_G)$ curve. Averages are obtained from 10 individual B -field sweeps.

-
- [1] Munning, F. *et al.* Quantum confinement of the Dirac surface states in topological-insulator nanowires. *Nat. Commun.* **12**, 1–6 (2021).
- [2] Ziegler, J. *et al.* Probing spin helical surface states in topological HgTe nanowires. *Phy. Rev. B* **97**, 035157 (2018).
- [3] Legg, H. F., Loss, D. & Klinovaja, J. Majorana bound states in topological insulators without a vortex. *arXiv preprint arXiv:2103.13412* (2021).
- [4] Ideue, T. *et al.* Bulk rectification effect in a polar semiconductor. *Nat. Phys.* **13**, 578–583 (2017).
- [5] Wang, Y. *et al.* Gigantic magnetochiral anisotropy in the topological semimetal ZrTe₅. *arXiv:2011.03329* (2020).
- [6] Liu, C.-X. *et al.* Model hamiltonian for topological insulators. *Phys. Rev. B* **82**, 045122 (2010).
- [7] Borgwardt, N. *et al.* Self-organized charge puddles in a three-dimensional topological material. *Phys. Rev. B* **93**, 245149 (2016).
- [8] Bömerich, T., Lux, J., Feng, Q. T. & Rosch, A. Length scale of puddle formation in compensation-doped semiconductors and topological insulators. *Phys. Rev. B* **96**, 075204 (2017).
- [9] Knispel, T. *et al.* Charge puddles in the bulk and on the surface of the topological insulator BiSbTeSe₂ studied by scanning tunneling microscopy and optical spectroscopy. *Phys. Rev. B* **96**, 195135 (2017).
- [10] Huang, Y. & Shklovskii, B. I. Disorder effects in topological insulator nanowires. *Phys. Rev. B* **104**, 054205 (2021).